International Journal of Heat and Fluid Flow 29 (2008) 1380–1392

Contents lists available at ScienceDirect

International Journal of Heat and Fluid Flow

journal homepage: www.elsevier.com/locate/ijhff

Head-on collision of shock wave induced vortices with a cylinder and a sphere

K. Kontis *, R. An, D. Kounadis, H. Zare-Behtash

University of Manchester, School of Mechanical, Aerospace and Civil Engineering, George Begg, P.O. Box 88, M60 1QD Manchester, UK

ARTICLE INFO

Article history:
Received 13 February 2007
Received in revised form 22 April 2008
Accepted 22 April 2008
Available online 11 June 2008

Keywords:
Shock-tube flows
Compressible vortex rings

ABSTRACT

An experimental study has been conducted to examine the interaction of shock wave induced vortices with a cylinder and a sphere. The experiments were carried out using a 30 mm internal diameter shock-tube, using air as both the driver and driven gas. High-speed schlieren photography was employed to study the development of the flow-field and the resulting interactions with the body configurations. Wall pressure measurements were also carried out to study the flow quantitatively along the leading edge of the cylinder. Three different diaphragm pressures ratios of 3.95, 7.89, and 11.84 were examined; the experimental shock Mach numbers were 1.28, 1.51 and 1.63, respectively. The experimental results indicate that as the incident shock wave impinges on the frontal surface of the cylinder or sphere, it undergoes transition from regular to Mach reflection. The induced flow-field due to the interaction of the vortex ring with the two models is highly three-dimensional and time dependent. The vortex ring attempts to engulf the sphere, whereas, in the case of the cylinder, part of the ring accelerates rapidly in the lateral direction along the leading edge of the body, whereas, the remaining flow moves around the cylinder. In both cases, the ring maintains its structure throughout the interactions.

1. Introduction

The flow-field induced by a shock wave impinging on convex surfaces has been studied both analytically and experimentally by a number of research groups (Heilig, 1969; Ben-Dor et al., 1980; Bryson and Gross, 1960). These studies have reported that as the shock wave propagates along the surface of the convex surface, the reflecting wedge angle at the reflection point decreases until the regular reflection goes through a transition to Mach reflection. Whitham (1957) has developed a two-dimensional theory for the diffraction and stability of shock waves, using the critical angle and the incident shock Mach number as initial values, to predict both the triple point locus and the development of the Mach stem. Heilig (1969), and Bryson and Gross (1960), who employed Mach-Zehnder interferometry and schlieren photography, respectively, reported that the agreement between Whitham's theory and experiment was satisfactory. Ben-Dor et al. (1980) reported that the analytical solutions, based on steady or pseudo-steady flows, over-predict the experimental results of the actual transition from regular to Mach reflection. More recently, Yang et al. (1987) employed computational calculations in order to study the diffraction pattern of a non-stationary shock wave after its impingement on a cylinder. The authors reported the subsequent development of the diffraction process, which was found to involve a regular reflection, transition to Mach reflection, Mach shock collision at the wake of the cylinder and complex shock–shock interactions. The numerical simulations were also compared with both the experimental work by Bryson and Gross (1960) and the theoretical calculations by Whitham (1957). The results indicated a good agreement with the previous researchers.

The interaction of a shock wave with a sphere has been investigated both experimentally and numerically by Tanno et al. (2003), and Sun et al. (2005). Tanno et al. (2003), who produced detailed pressure data along the apex of a sphere, reported a maximum pressure at the frontal stagnation point, which decreases with decreasing wall inclination angles. The authors also reported high pressure levels at the rear of the sphere because of the Mach shock collision at the wake of the sphere. Sun et al. (2005) studied the unsteady drag of a sphere, produced by a shock Mach number of 1.22. It was reported that the sphere experiences a steep drag increase immediately after shock impingement and reflection from the frontal side. Then, the drag was found to drop as the shock wave moves to the rear side of the sphere and finally converges to a nearly constant value.

The flows and interactions associated with compressible vortex rings have received very little attention, and there are still many unanswered questions related to most aspects of the vortex rings themselves, including their formation, propagation and decay, with more challenging complexities in both their dynamics and energetics introduced by the effects of compressibility (Kontis et al., 2006). The present study examines the flow-field produced when a shock wave and the induced-vortex ring approach and impinge on a cylinder and a sphere. It forms part of a larger research effort contributing

* Corresponding author. Tel.: +44 161 3065751.
E-mail address: k.kontis@manchester.ac.uk (K. Kontis).

0142-727X/$ - see front matter © 2008 Elsevier Inc. All rights reserved.
doi:10.1016/j.ijheatfluidflow.2008.04.010

directly into the future advances of non-lethal-weapon, fluid dynamics and high speed technology. The project will also benefit those concerned with developing and validating DNS/LES and RANS simulation tools. The effects of compressibility are identified with respect to the strength of the generating shock wave at the exit of the shock-tube. The present investigation visualises the flow-field using time-resolved schlieren photography, and it identifies the strength of the various interactions using wall pressure measurements.

2. Apparatus and instrumentation

Experiments have been carried out using a cylindrical shock-tube (Fig. 1) made of seamless pipe. The internal (d_i) and external (d_o) diameters of the shock-tube were 30 mm and 38 mm, respectively. Experiments have been performed for diaphragm pressure ratios of 3.95, 7.89 and 11.84, with air as both driver and driven gas, producing shock Mach numbers of 1.28, 1.51 and 1.63, respectively. The three Mach numbers were chosen because of the distinct flow regimes that each one creates. From $M = 1.0$ to 1.43, conventional-looking vortex rings are produced characterised by very thin cores. From $M = 1.43$ to 1.60, the axial flow velocity in the recirculating region of the vortex ring becomes supersonic, producing rearward-facing shock wave embedded in this region. From $M = 1.60$ to 2.0, a secondary counter-rotating vortex ring forms ahead of the main vortex ring (Brouillette and Hebert, 1997; Kontis et al., 2006).

The pressure in the driven section was atmospheric. The length of the driver and the driven sections were $100d_i$ and $43.68d_i$, respectively. An industrial film diaphragm has been used to divide the two sections in the shock-tube. The thickness of the diaphragm was chosen to be 23, 55 and 75 μm for the case of 3.95, 7.89 and 11.84 pressure ratios, respectively. The bursting of the diaphragm was initiated manually with a plunger.

A cylinder and a sphere were employed to study the interaction effects of the incident shock wave and the induced-vortex ring. Both models were designed to be 30 mm in diameter and were placed 80 mm in front of the shock-tube exit plane. These geometric parameters were determined from previous experimental work on the rate of growth and propagation of a compressible vortex ring (Kontis et al., 2006). The central axis of both the cylinder and the sphere were aligned with the axis of symmetry of the shock-tube. In the case of the cylinder, measurements were carried out with its axis both horizontal and vertical to the shock-tube. The dimensions of the models are shown in Fig. 2.

High-speed schlieren photography (Settles, 2001; Merzkirch, 1974) was employed to visualise the flow formed at the open end of the shock-tube and the induced interactions. Fig. 3 shows the actual arrangement of the schlieren system. Side-view images

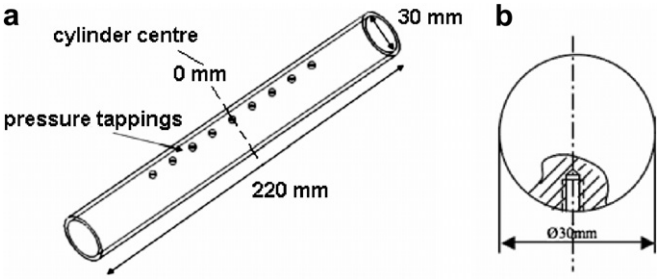

Fig. 2. Dimensions of the models: (a) cylinder and (b) sphere.

were captured, utilising an Argon stabilised pulsed flash system (625 ns duration, 5 J) as a light source. The light generated by the flash passes through a plano-convex lens (75 mm in diameter and 75 mm focal length) and the converged light spot passes through a variable iris (3 mm–50 mm) and cut by a slit. Then, the resulting light beam reaches a parabolic mirror of 203.3 mm diameter and 1016 mm focal length. The collimated light beam passes through the test region and then is focused by another parabolic mirror. The focal point of the mirror is on a knife edge. The flash lamp was triggered by one of the transducers (Kulite XT-140) mounted on the shock-tube, and located $22.017d_i$ from the diaphragm, see Fig. 1. Then, the flow features, in time sequence, were built-up by delaying the emission of the flash using the signal synchronisation unit. The resolution of the combined system had a limit of 40 kHz. The experiments were carried out in dark conditions. The photographs were taken using a large format camera with 4×5 in. ISO100 black and white Polaroid film.

Wall pressure measurements were conducted along the leading edge of the cylinder at different locations away from its centre, 0, ±16, ±32 and ±48 mm, see also Fig. 2. Pressure transducers (Kulite XT-140) connected to flexible tubes, were mounted inside the cylinder. The delay of the signal for each Mach number was calculated and subtracted from the original signal, in order to match the flow features visible from the schlieren images with the corresponding pressure values obtained from the pressure measurements.

The transducers were firstly calibrated, based on the existing calibration facility, for a range of pressures between 0 and 5 bar. The signal from each transducer was transmitted to a PC equipped with a high-speed Data Acquisition System (NI PCI-6251), via a signal conditioner (NI SCXI-1520). The combined system had the capability of collecting data in a frequency up to 40 kHz. The transducer (Kulite XT-140) mounted onto the shock-tube and located $22.017d_i$ from the diaphragm, was used to trigger the collection of the data, see Fig. 1. The data were recorded and stored by means of the existing software (LABVIEW). The stored data was then processed using a commercial software (Matlab). The repeatability er-

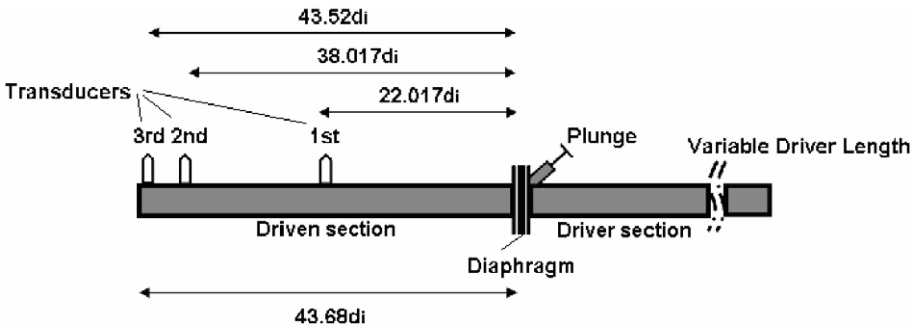

Fig. 1. Schematic diagram of the shock-tube.

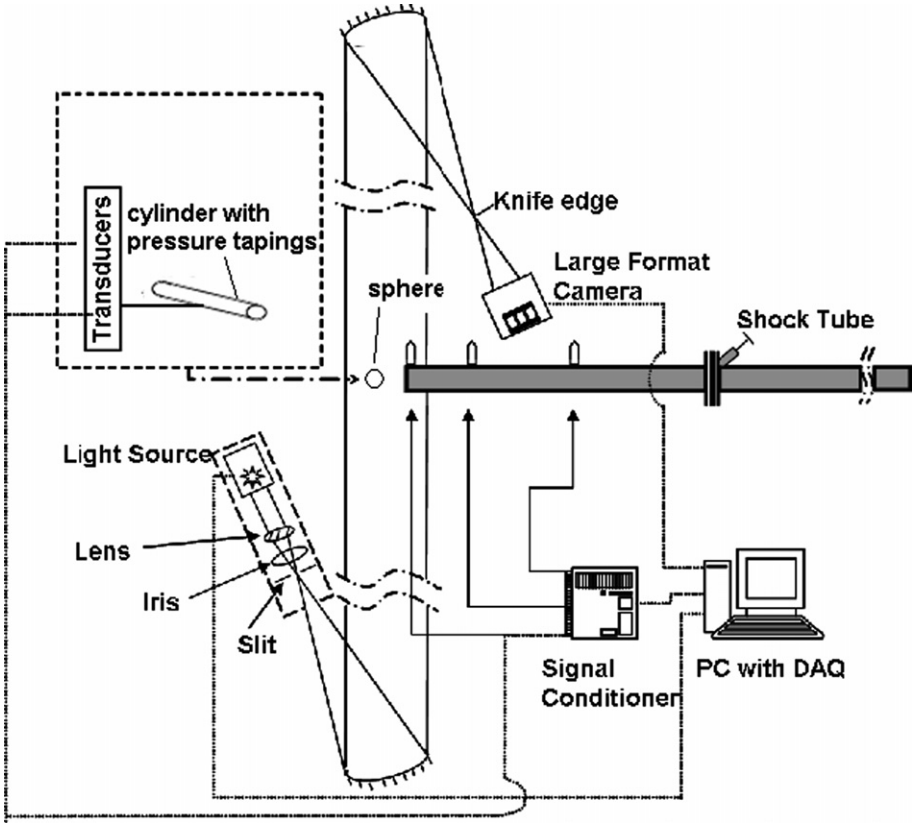

Fig. 3. Schematic diagram of the set-up used for the schlieren measurements.

ror was 2% and 1% for all pressure measurements and schlieren pictures, respectively.

3. Flow-field characteristics (without cylinder and sphere)

3.1. Shock wave calculations inside the shock-tube

The shock wave velocity for all the cases examined, was obtained using the signals from the pressure transducers, mounted on the wall in the driven section of the shock-tube. The shock velocity (U_s) in the tube was obtained from the distance between the transducers (denoted as 1, 2, and 3 in Fig. 1) and the time between the pressure peaks in the measured signal corresponding to the passage of the shock wave. The incident shock Mach number (M_s) was then calculated for each of the driver pressures, under maximum driver length of $100d_i$. The theoretical Mach numbers corresponding to each diaphragm pressure ratio were calculated following the procedure described by Kontis et al. (2006). The temperature in the driver and driven sections was assumed ambient (300 K). The maximum driver length was selected in order to produce shock waves with maximum strength (Kontis et al., 2006).

Table 1 gives the experimental conditions and the corresponding shock velocities and Mach numbers at various locations inside the shock-tube, where U_{s1} and U_{s2} represent the shock velocities between transducers 1 and 2, and transducers 2 and 3, respectively. It is clear that the shock wave velocity is higher near the tube exit, for all the diaphragm pressure ratios (P_4/P_1) examined. Subscripts 1 and 4 refer to the initial conditions behind and ahead of the diaphragm. The velocity increase is attributed to the fact that, immediately after the diaphragm rupture, a shock front is formed due to the coalescing of the compression waves, which gains strength until it reaches a maximum velocity (Glass and Sislian, 1994; White, 1958). It is believed (Emrich and Curtis, 1953; Emrich and Wheeler, 1958; Bleakney et al., 1949) that if the diaphragm is not stressed to its limit before it is punctured, the shock velocity may increase before starting to decrease. The shock wave is fully formed several tube diameters downstream of the diaphragm. Shugaev and Shtemenko (1998) have reported that the maximum value of shock velocity depends on the rate of the diaphragm-opening at initial instants. The less the rate of opening, the less the influence in the maximum value of the shock velocity and the greater the formation distance.

Table 1
Comparison between experimental and theoretical calculations

Experimental					Theoretical		
P_4/P_1	U_{s1} (m/s)	U_{s2} (m/s)	M_{s1}	M_{s2}	P_2/P_1	U_s/(m/s)	M_s
3.95	389.33 ± 6.1	448.73 ± 3.9	1.13	1.28	1.92	458.56	1.34
7.89	434.89 ± 5.8	511.00 ± 6.7	1.27	1.51	2.58	526.94	1.54
11.84	494.47 ± 3.6	552.42 ± 6.0	1.44	1.63	3.05	569.55	1.66

The theoretical values of the shock velocity (U_s), shock Mach number (M_s) and shock wave strength ($\xi = P_2/P_1$) are shown in Table 1, where P_2 is the pressure behind the shock wave. It is evident that the theoretical values are closer to the experimental values corresponding to the pressure measurements taken near the exit of the shock-tube. However, their magnitude is slightly higher than the experimental ones. The difference between experimental and theoretical values is due to the fact that the one-dimensional theory assumes instantaneous diaphragm bursting reducing the problem to the break-up of an arbitrary discontinuity. In addition, by assuming that the subsequent flow is one-dimensional, adiabatic and inviscid, interactions with the wall of the tube are neglected. The amount of the discrepancy mainly depends on the location of the measuring station.

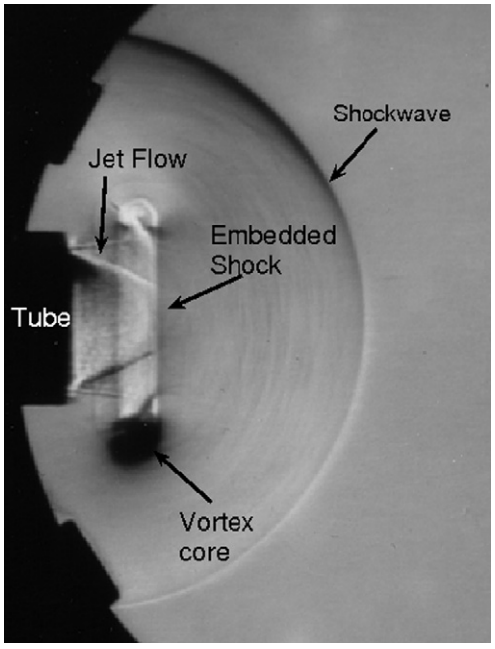

Fig. 4. Shock wave and vortex ring at a shock Mach number of 1.63.

3.2. Shock wave propagation outside shock-tube

The shock wave that is emitted from the open end of the shock-tube is diffracted at the nozzle exit and as it travels, becomes spherical (Fig. 4). In order to examine the axial development of the shock wave as it exits the tube, a number of schlieren photographs were digitized and the intensity profiles were obtained using Matlab. Fig. 5 shows typical intensity profiles along the axis of symmetry of the flow-field at different specified times, for the case of $M_s = 1.51$. By measuring the distance in pixels between points A, B, C and D, the position of the shock wave relative to the shock-tube could be determined.

Fig. 6 shows the distance propagated by the shock wave as a function of time, for $M_s = 1.28$, 1.51 and 1.63. The time is based on the transducer located at $43.52d_i$ from the diaphragm. The error in the values was calculated to be approximately 5%. The error takes into consideration the resolution of the system, the imperfections in the flow due to the diaphragm-opening process and the error due to the image processing. As it is expected, with increasing shock Mach number, the shock wave covers a greater distance at the same time. The relatively linear distribution of the data points in each case suggests that the shock wave is propagating with a constant speed.

3.3. Vortex ring propagation

Immediately after the shock is emitted, the gas within the shock-tube starts to be discharged. Consequently, the shear layer, which is generated between the emerging and external fluids, starts to roll-up and then, develops a strong vortex ring near the open end. Fig. 4 shows the vortex ring, which is described by the dark/bright region at the centre of its core.

As the vortex ring propagates downstream, an embedded shock wave (Fig. 4) appears to be formed in the vortex ring. This observation is consistent with previous studies (Kontis et al., 2006; Brouillette and Hebert, 1997). The schlieren pictures indicate that the generated embedded shock wave travels with the main ring, as it accelerates downstream. The presence of the embedded shock wave could be attributed to the fact that the induced flow velocity in the region of the ring becomes supersonic in the frame of reference of the ring. Behind the vortex ring, a jet flow with a typical oblique shock pattern is generated. The generation of the oblique shock pattern, which develops a diamond structure, was found (Kontis et al., 2006), to be the result of the acceleration of the

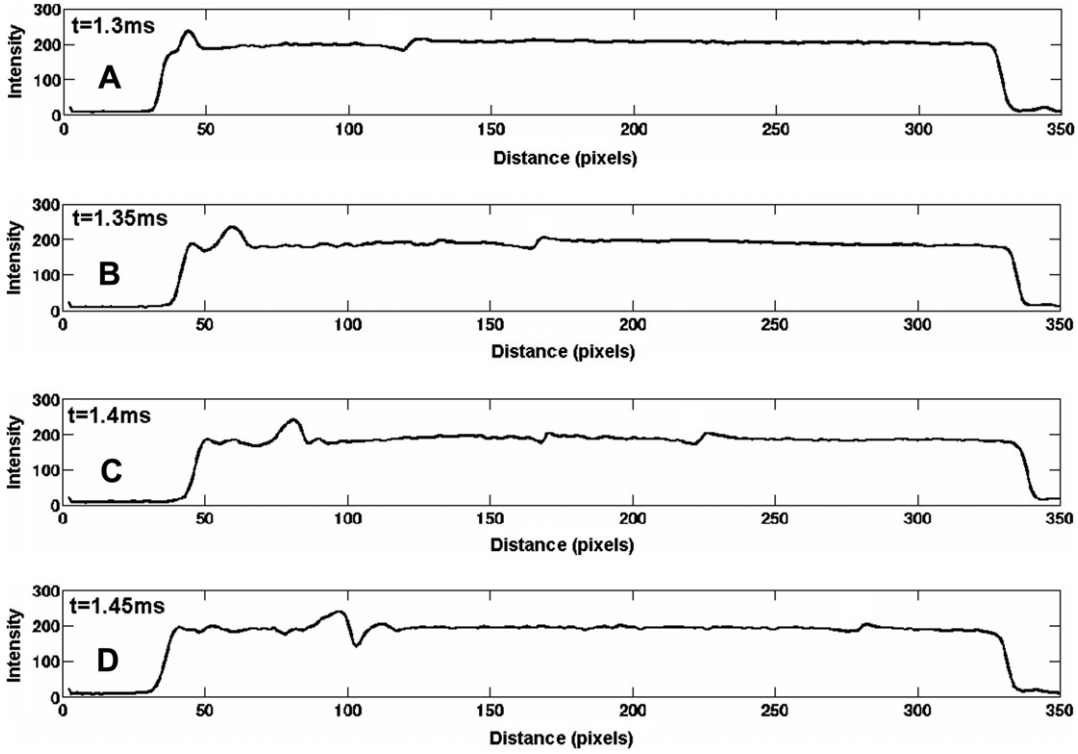

Fig. 5. Intensity profiles along the axis of symmetry of the flow-field at different times at a shock Mach number of 1.51.

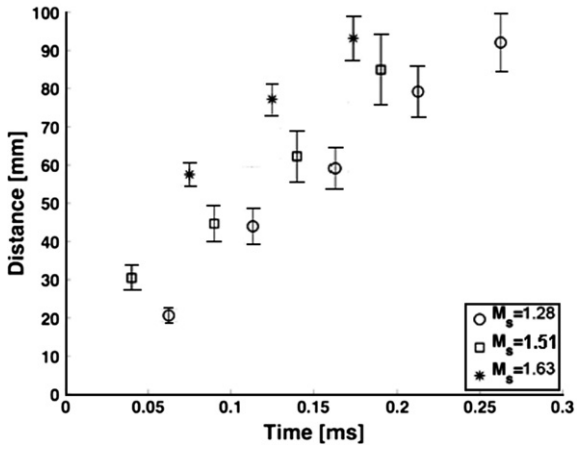

Fig. 6. Distance propagated by the shock wave as function of time at different shock Mach numbers.

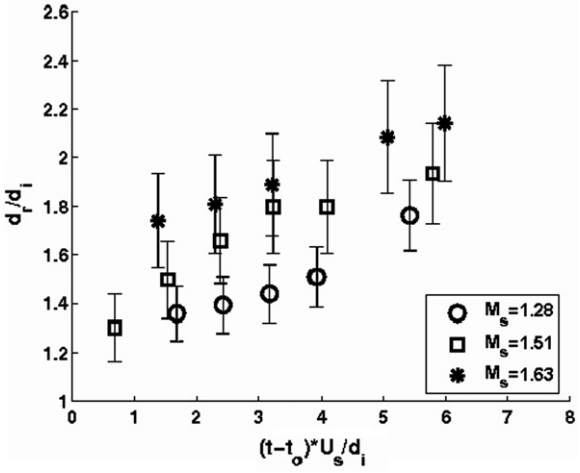

Fig. 8. Variation of vortex ring diameter with time at different shock Mach numbers.

expansion waves inside the shock-tube. At some distance further downstream of the tube exit, the vortex ring system leaves the oblique shock structure; an observation which is consistent with that of Baird (1987).

Ring diameter, d_r and core diameter, d_c are two important geometric parameters, which characterise a vortex ring. In order to determine these quantities, the schlieren photographs were digitized and the intensity distributions were processed using Matlab, in a similar way to that described in Section 3.2. The error in the variation of the geometric parameters was calculated to be 5%.

Fig. 7 shows the variation of the dimensionless position of the vortex ring, L/d_i, with dimensionless time $(t-t_o) \times U_s/d_i$, for the three Mach numbers. The dimensionless time $(t-t_o) \times U_s/d_i$ is based on the specified time t, the time required for the shock wave to reach 5 mm from the tube exit, t_o, the corresponding shock wave velocity U_s and the inner diameter d_i of the tube. The measurement of both t and t_o is using as reference the transducer located $43.52d_i$ from the diaphragm (t_o is the time that takes for the shock wave to reach the third transducer, which is located 5mm from the tube exit). The results indicate that initially, during the formation stage, the vortex ring propagates at a slow rate. As the vortex ring accelerates the propagation distance increases significantly with time. The location of the maximum velocity value is found to occur at a distance equal to the tube diameter, an observation consistent with that of Arakeri et al. (2004). Elder and De Haas (1952) have reported that the vortex ring retains its velocity until it is reached by the expansion waves from inside the tube. Then, according to those authors, the ring velocity starts to decay to a constant velocity.

The growth of the vortex ring diameter is shown in Fig. 8. It is found that the vortex ring diameter increases with time and the rate of growth of d_r/d_i follows a linear trend. The variation of the vortex core diameter with time is shown in Fig. 9. It is evident that the diameter of the vortex core is a non-linear function of time. In addition, the vortex core is found to increase in diameter as it moves downstream, due to the diffusion of vorticity. However, for the two lower shock Mach numbers, the core diameter seems to asymptote at earlier times than that for the higher shock Mach number. This could be an indication of the lower rate of dissipation of the vortex ring with decreasing diaphragm pressure ratio. At lower shock Mach numbers, the vortex ring is more stable including its core and travels greater distances, making it easier to be traced in the schlieren images. However, at higher Mach numbers the ring develops azimuthal instabilities much quicker and entrains ambient fluid at a greater rate which increases the outer core fluid region and causes it to continue to grow (Kontis et al., 2006). In addition, schlieren studies by Kontis et al. (2006) have shown that if the diaphragm pressure ratio is kept constant the dissipation rate of the vortex ring increases with increasing distance from the tube exit.

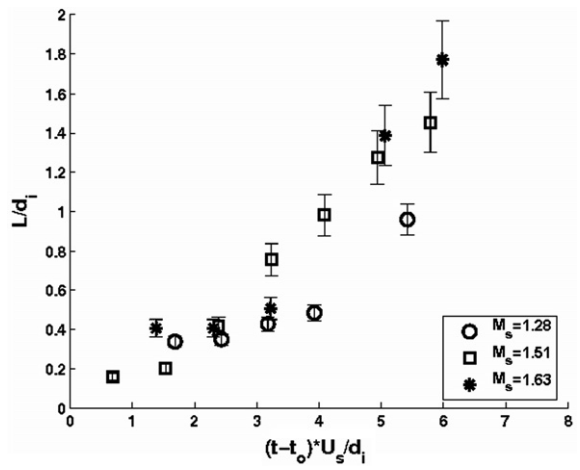

Fig. 7. Variation of vortex ring position with time at different shock Mach numbers.

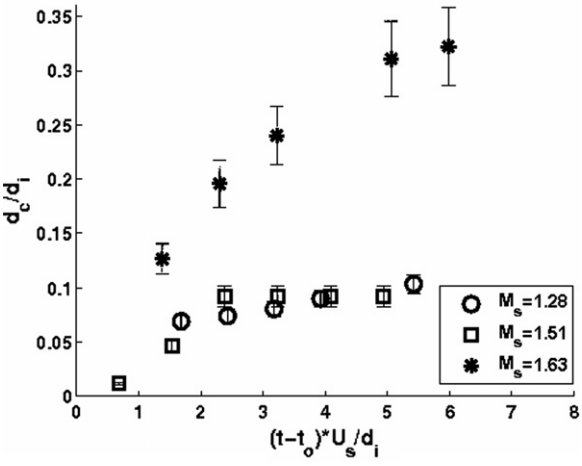

Fig. 9. Variation of vortex core diameter with time at different shock Mach numbers.

4. Flow-field characteristics (with cylinder and sphere)

4.1. Shock wave interaction with cylinder and sphere

When the incident shock wave impinges on the cylinder, it first experiences a head-on collision and immediately develops a two-shock system referred to as a regular reflection (Fig. 10a). The coincidence point travels along the cylinder surface. As the shock wave propagates along the surface of the cylinder, the 'local equivalent wedge angle' at the reflection point decreases until a critical value, where the regular reflection transits into irregular reflection in the form of a single Mach reflection. Similar observations have been

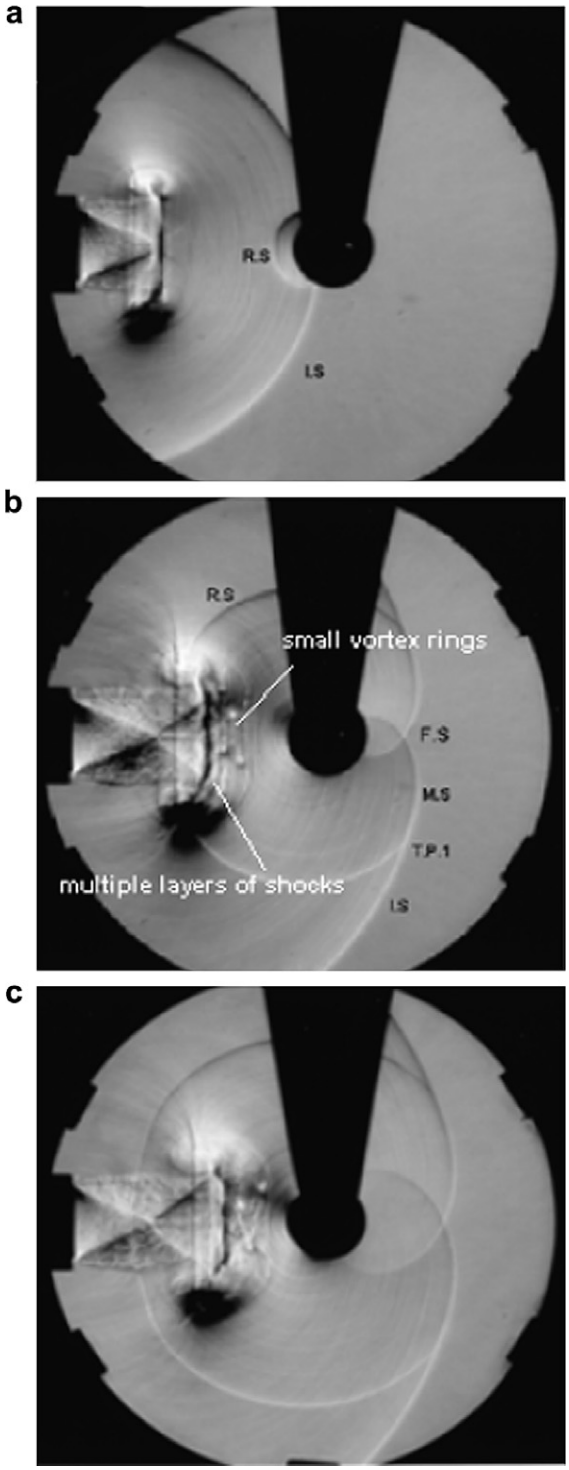

Fig. 10. Shock wave interaction with the cylinder at (a) 1.2 ms, (b) 1.3 ms and (c) 1.35 ms for a shock Mach number of 1.63. Notation: R.S., reflected shock, I.S., incident shock, M.S., Mach shock, T.P.1., Mach shock triple point and F.S., focusing shock.

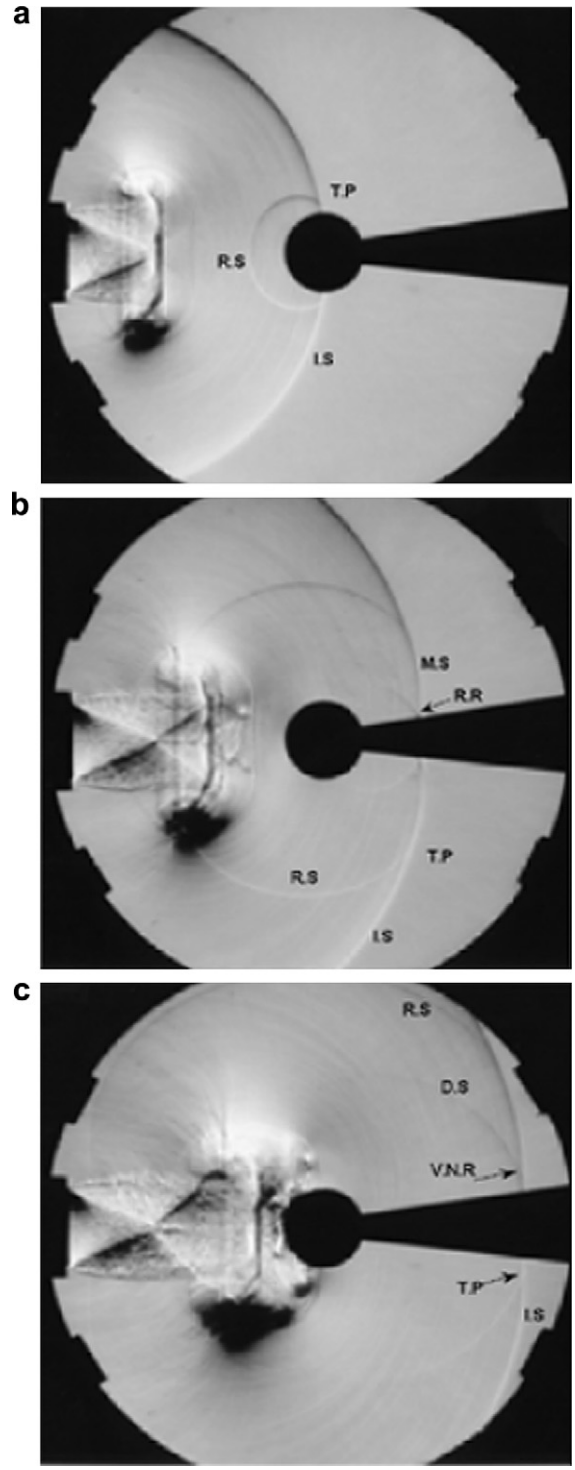

Fig. 11. Shock wave with the sphere at (a) 1.2 ms, (b) 1.3 ms and (c) 1.4 ms for a shock Mach number of 1.63. Notation: T.P., Mach shock triple point, F.S., focusing shock, R.R., regular reflection, D.S., diverging shock and V.N.R., von Neumann reflection.

made from previous studies by Gonor et al. (2004), Yang et al. (1987), Bryson and Gross (1960), Heilig (1969), and Ben-Dor et al. (1980).

Fig. 10b and c show the subsequent development of the flowfield. The Mach reflection consists of a three-shock system, namely the incident shock, the reflected shock and the Mach stem. The incident and reflected shocks are no longer meeting at the wall but rather at a triple point with a new shock front, the Mach stem and a slip stream, which is a contact discontinuity but it is not evident in the present images. As the incident wave propagates further downstream, complex shock–shock interactions occur as the Mach shocks collide behind the cylinder. Downstream of the cylinder, a shock focus is formed due to the complicated flow interactions. Fig. 10b indicates the presence of a focusing shock (F.S.) resulting from the point of collision of the converging cylindrical Mach shock at the rear stagnation point of the cylinder.

From Fig. 6, it can be estimated that the shock wave velocity outside the shock-tube, corresponding to a diaphragm pressure ratio of 11.84 (M_s = 1.63 inside the tube), leads to an incident Mach number of 1.16 (assuming ambient temperature conditions). This estimation is consistent with the fact that shock wave does not induce a velocity just downstream the shock (in the shock wave reference), and could explain the fact that no vortex shedding in obtained at the back of the cylinder (in contrast to previous studies, for example by Yang et al. (1987)). The characteristic time scales required for the development of vortex shedding must be taken into account. The lack of indication of vortex shedding may be due to the fact that the flow is in transient process.

Similar to the cylinder case, when the incident shock wave impinges on the frontal side of the sphere, a regular reflection is formed. Then, the shock wave system transits from regular to Mach reflection (Fig. 11a). Mach reflection is created at small 'local

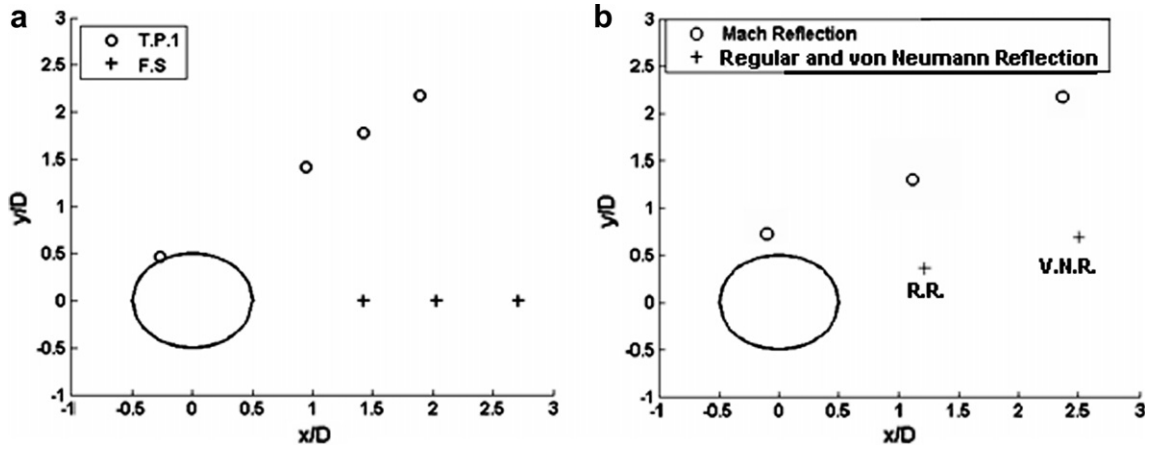

Fig. 12. Trajectories of the various interaction points along (a) cylinder and (b) sphere for a shock Mach number of 1.63.

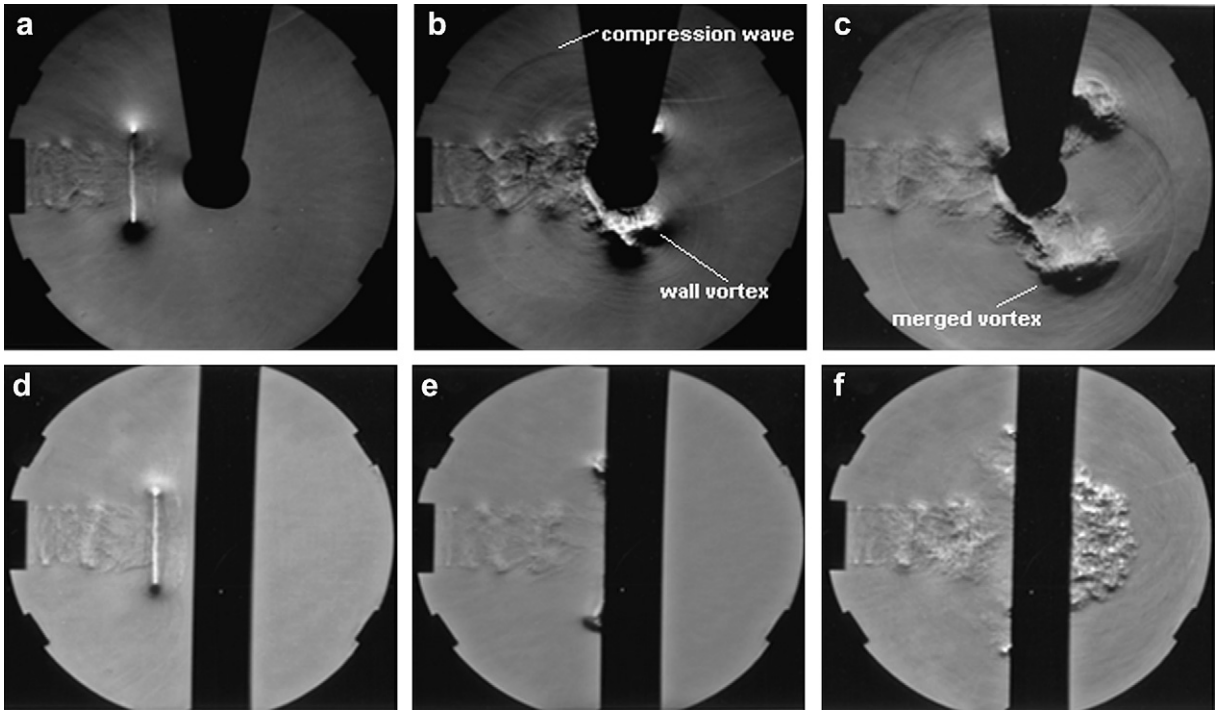

Fig. 13. Schlieren photographs showing the interaction of the vortex ring with the cylinder; horizontal direction at (a) 2.0 ms, (b) 2.2 ms and (c) 2.4 ms, and vertical direction at (d) 2.0 ms, (e) 2.2 ms and (f) 2.4 ms for a shock Mach number of 1.28.

equivalent wedge angles', when a reflected shock wave cannot deflect the stream to become parallel to the wall. Behind the sphere, the flow-field behaviour is altered from the presence of the holder, which acts as a wedge. As the resulting shock impinges on the holder, a new regular reflection is generated. Then, further downstream, the regular reflection transits into an irregular reflection in the form of a von Neumann reflection rather than a Mach reflection (Fig. 11c). The difference between the single Mach reflection and the von Neumann reflection is that the former has continuous curvatures over the entire shock front including an incident shock

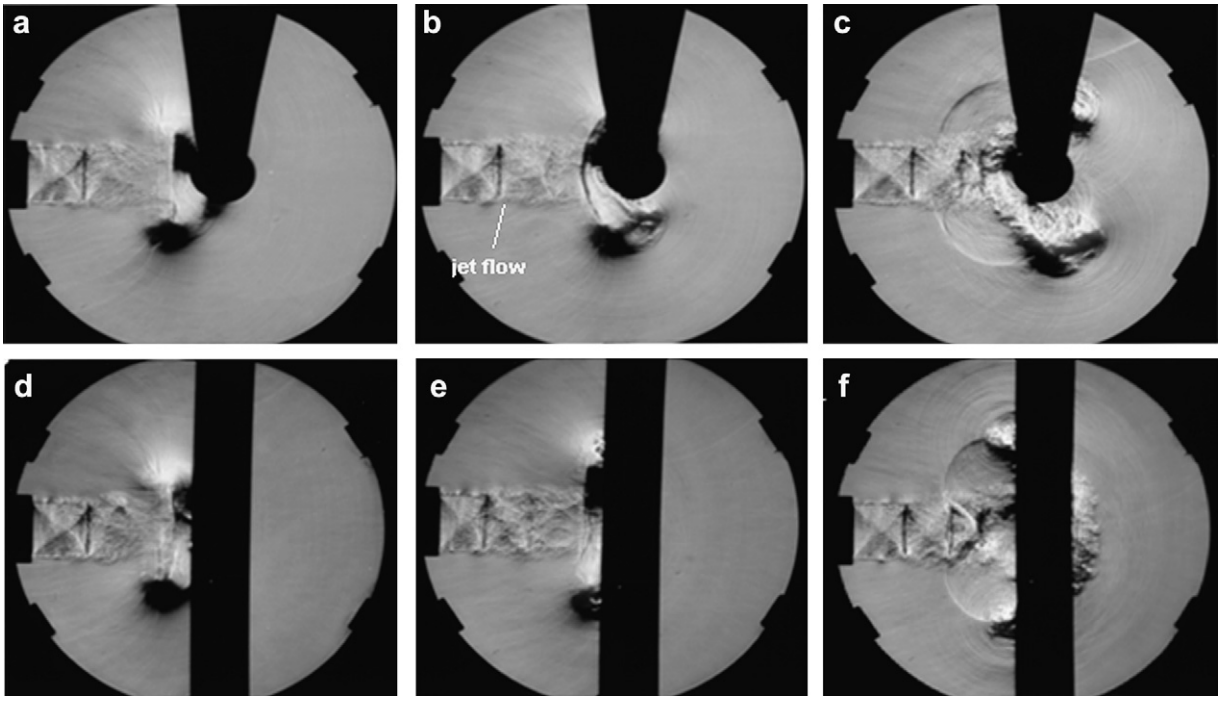

Fig. 14. Schlieren photographs showing the interaction of the vortex ring with the cylinder; horizontal direction at (a) 1.6 ms, (b) 1.7 ms and (c) 1.8 ms and vertical direction at (d) 1.6 ms, (e) 1.7 ms and (f) 1.8 ms for a shock Mach number of 1.51.

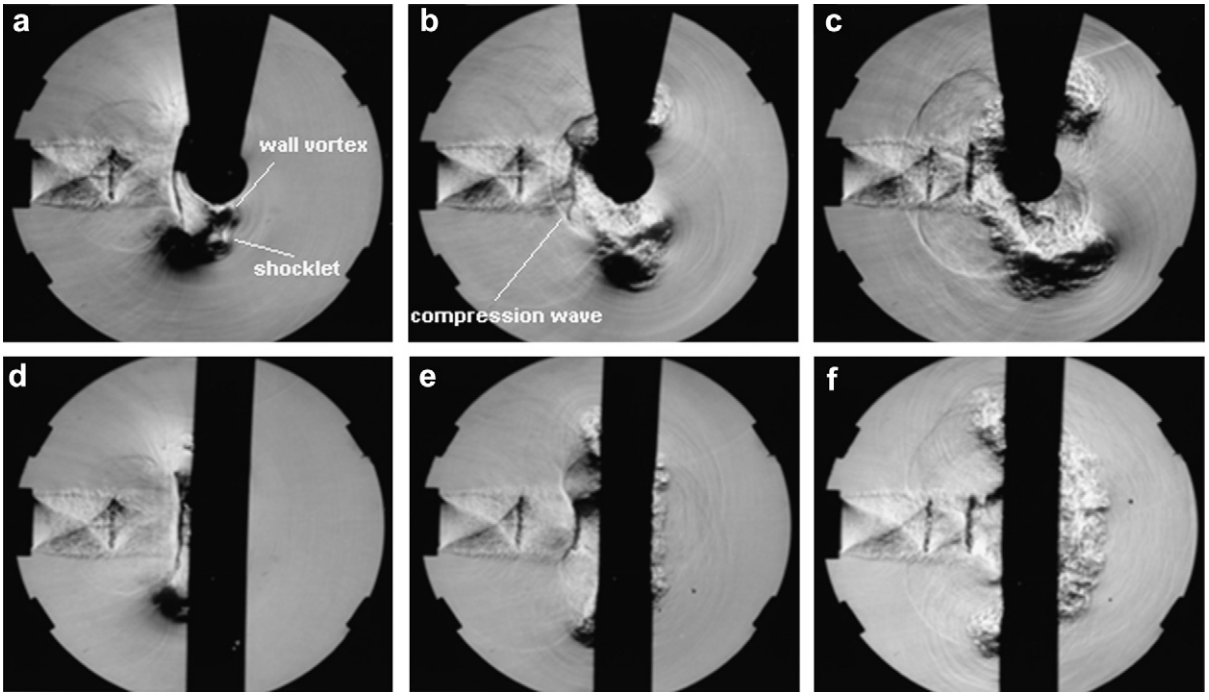

Fig. 15. Schlieren photographs showing the interaction of the vortex ring with the cylinder; horizontal direction at (a) 1.5 ms, (b) 1.6 ms and (c) 1.7 ms and vertical direction at (d) 1.5 ms, (e) 1.6 ms and (f) 1.7 ms for a shock Mach number of 1.63.

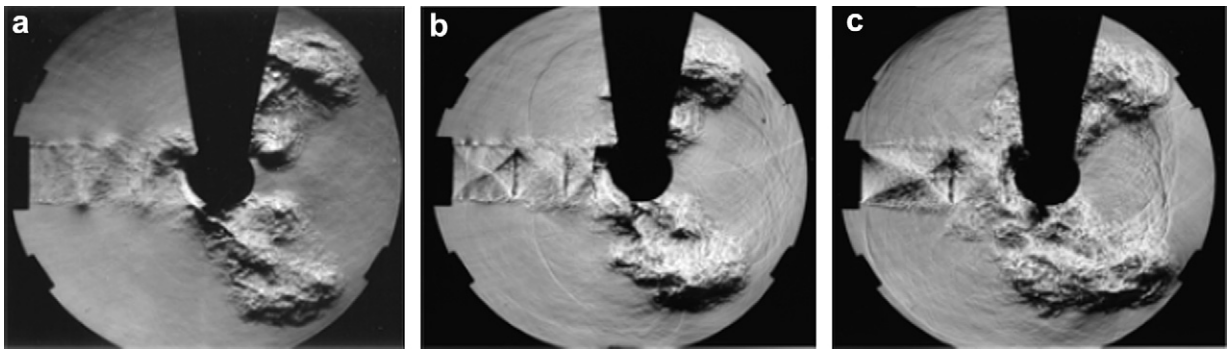

Fig. 16. Schlieren images showing the interaction of the vortex ring with the cylinder placed in the horizontal direction for (a) $M_s = 1.28$ and t = 2.6 ms, (b) $M_s = 1.51$ and $t = 2.0$ ms and (c) $M_s = 1.63$ and $t = 1.8$ ms.

and a Mach stem, while the latter has a curvature discontinuity at the triple point (Ben-Dor, 1992).

In the case of the impact of the shock wave with the cylinder, the resulting trajectories of the Mach shock triple point along with the focused shock are presented in Fig. 12a. Due to the symmetry of the flow, half of the diffraction pattern is shown. There is an almost linear variation of the triple point, relative to the location of transition. According to Fig. 12a transition between regular and Mach reflection occurs at an incident angle of 57.77°. It should be noted that the existing analytical, experimental and computational data are referred to plane incident shock waves. In the present study, the incident shock wave has a spherical shape, which is a truly unsteady case, and this could probably affect the location of initiation of the Mach reflection. As the converging shocks at the cylinder wake continue to pass one-another, the position of their focus remains stationary in the transverse direction while moving further downstream. Fig. 9b shows the propagation of the Mack shock reflection, and the locations of the regular reflection and then von Neumann reflection in the region close to the holder, for the case of the shock wave impingement on the sphere.

4.2. Vortex ring interaction with cylinder and sphere

4.2.1. Cylinder

The initial shock wave emitted from the shock-tube collides and reflects from the front side of the cylinder (Fig. 10a). Then, the reflected shock wave impinges on the vortex ring and its shape is deformed. As the reflected shock wave travels through the vortex ring, its central portion is captured by the vortex ring (Fig. 10b). The outer portion of the reflected shock wave is diffracted in the vortex core and bends as it passes around the core. The above description agrees with the experimental work of Tokugawa et al. (1997). The interaction of the vortex ring with the reflected shock is more pronounced for the higher shock Mach number examined. For $M_s = 1.63$, the generation of multiple layers of shock waves between the embedded shock and the cylinder, can be observed (Fig. 10b and c). In addition, small vortex rings, with reverse circulation, are generated due to the roll-up of the shear layer ahead of the main vortex.

Figs. 13–15 show the flow development with time as the vortex ring approaches and interacts with the cylinder. The cylinder was placed both horizontally and vertically to the oncoming flow to allow visualization of the interaction. The schlieren images indicate that as the vortex ring approaches the cylinder, the flow between the ring and the body starts to compress (Figs. 13, 14 and 15a). The compression continues to build up until it reaches a critical point, and a compression wave is formed travelling back towards the shock-tube exit. The strength of this wave is found to increase with increasing shock Mach number (Figs. 13c, 14c and 15c). The

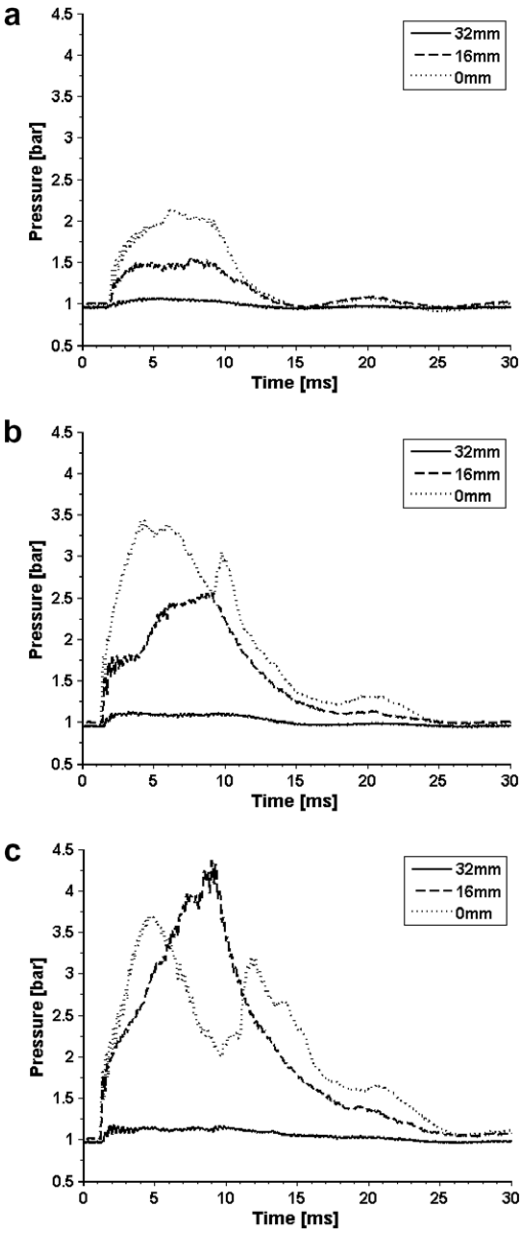

Fig. 17. Pressure variations during the total running time of the shock-tube corresponding to tapings located at different locations along the apex of the cylinder at shock Mach number of (a) 1.28, (b) 1.51 and (c) 1.63.

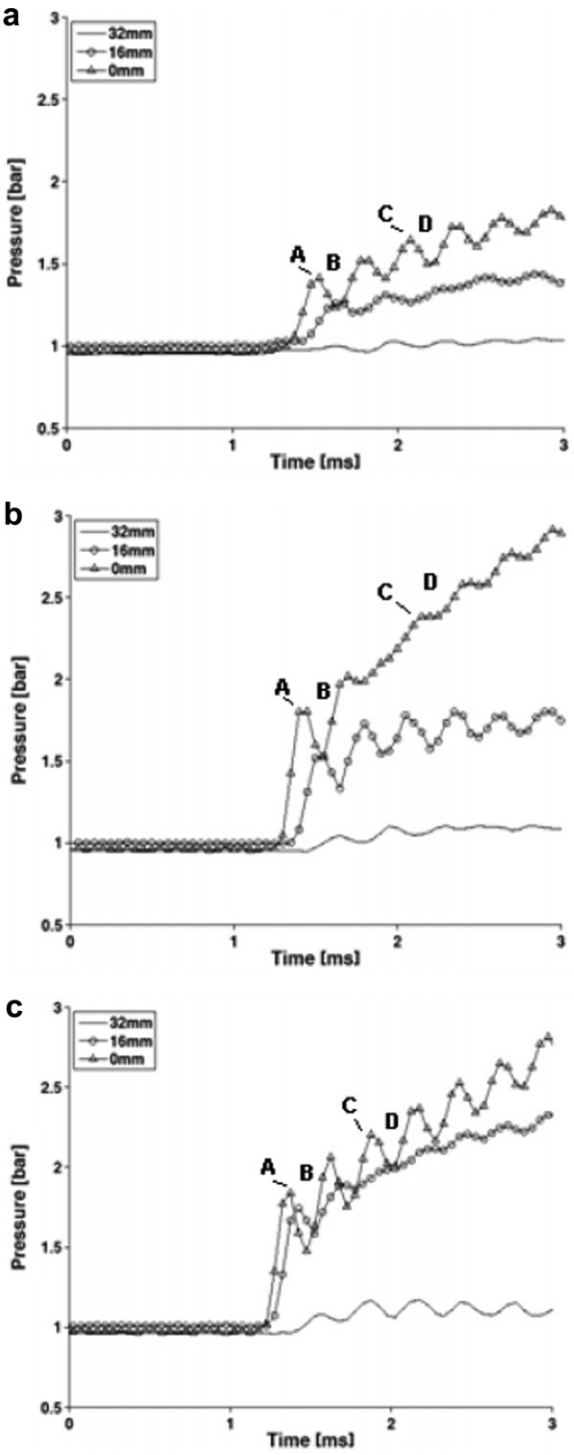

Fig. 18. Pressure variations corresponding to tapings located at different locations along the apex of the cylinder for the first 3 ms of measurement at shock Mach number of (a) 1.28, (b) 1.51 and (c) 1.63.

resulting wave intersects the vortex ring and diffracted waves are generated. The diffracted waves interact with the vortex core and start to disturb its shape. In the horizontal direction, the main vortex ring moves around the cylinder (see for example Figs. 13b and c, 14b and c, 15b and c), and its propagation path remains initially almost undisturbed. In the vertical direction, the vortex ring starts to expand laterally along the leading edge of the cylinder (Figs. 13e, 14e and 15e). This flow behaviour is present for all Mach number cases examined, and it becomes more pronounced with increasing compressibility. As the jet flow, which follows the main vortex ring, approaches the cylinder, the flow-field becomes even more complicated. The flow in the region around the cylinder is firstly compressed because of its interaction with the oncoming flow and then it is subjected to expansion as the jet is reflected backwards. This flow behaviour is repeated as the oncoming jet flow approaches the frontal side of the cylinder. The resulting flow around the cylinder surface starts to interact with the vortex core, weakening its strength and coherence. This results in a rapid distortion of the vortex ring shape. The strong disturbance of the vortex ring is evident from the schlieren images, which are taken with the cylinder placed in the horizontal direction. Figs. 13c, 14c and 15c show that the flow rapidly becomes turbulent. At longer times (Fig. 16), the turbulent ring expands further and a highly complicated flow-field develops, which is accompanied by the emission of acoustic waves.

Pressure measurements were carried out by placing a number of tapings along the leading of the cylinder. The location of these tapings is shown in Fig. 2a, and it is described in Section 2. The wall pressure measurements are presented as pressure variations with time of the individual tapings. Due to symmetry of the flow, only the data from the half of the cylinder are plotted. The measurement of time is using as reference the instant when the incident shock wave passes the transducer located $22.017d_i$ from the diaphragm (Fig. 1).

Fig. 17 shows the variations for the three different shock Mach numbers during the total running time of the shock-tube. In order to better understand how the flow development affects the wall pressure levels, a closer look was undertaken on the pressure profiles by plotting only the first 3 ms of the original signal (Fig. 18). The pressure profiles in the stagnation region can be divided into three regions. The first region (0–3 ms) is characterised by an initial sharp peak, which corresponds to the arrival of the shock front (Fig. 18), followed up by a series of consecutive pressure fluctuations of increasing magnitude associated with the interaction of the vortex ring with the cylinder, the compression of the flow between the ring and body, and the formation of the reflected compression wave. In the second region (3–6 ms) (Fig. 17), the pressure levels reach a maximum value, due to the combined effects of the reflected compression wave and jet flow behind the ring. The third region (6–30 ms) is identified by fluctuations of pressure of decreasing magnitude, which correspond to different flow phenomena mainly due to the interaction of the jet with the cylinder, indicating dissipation of the flow-field. Figs. 17 and 18 show that the strength of the incident and reflected waves and of the resulting flow interactions increases with increasing shock Mach number.

Regarding the signal obtained from the central transducer (Fig. 18), the pressure value, which is denoted as A, corresponds to the time that the effect of the shock front ends. Then, as the shock wave is reflected, the pressure behind it, increases resulting in a further increase of the wall pressure reaching a maximum value of 1.41 bar at 1.52 ms, 1.8 bar at 1.4 ms and 1.84 bar at 1.32 ms, for M_s = 1.28, 1.51, and 1.63, respectively. The increase of the pressure at the wall, due to the reflection, confirms the presence of a strong shock (Courant and Friedrichs, 1948; Von Neumann, 1963). The pressure levels start to drop for the next 0.2 ms (time B) (Fig. 18). The pressure drop could be attributed to the lateral acceleration of the flow away from the stagnation region. For the next 0.5 ms, up to time C, a number of strong pressure fluctuations occur at the stagnation region. These significant pressure variations could be attributed to the interaction between the existing fluid near the wall and the oncoming flow, as it is shown in Figs. 13–15. The fluid at the wall is initially compressed resulting to the generation of reflected waves, affecting significantly the wall pressure levels. The sharp increase of the pressure levels indicates

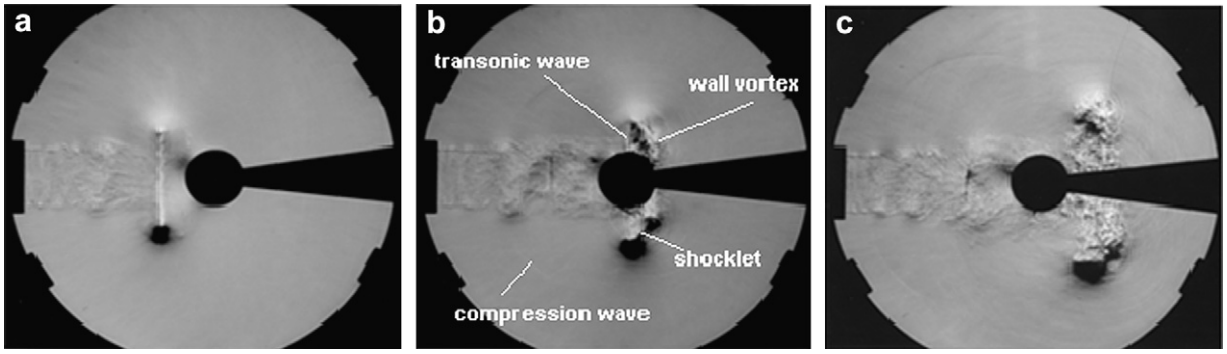

Fig. 19. Schlieren images showing the interaction of the vortex ring with a sphere at (a) 2.0 ms, (b) 2.2 ms and (c) 2.4 ms for a shock Mach number of 1.28.

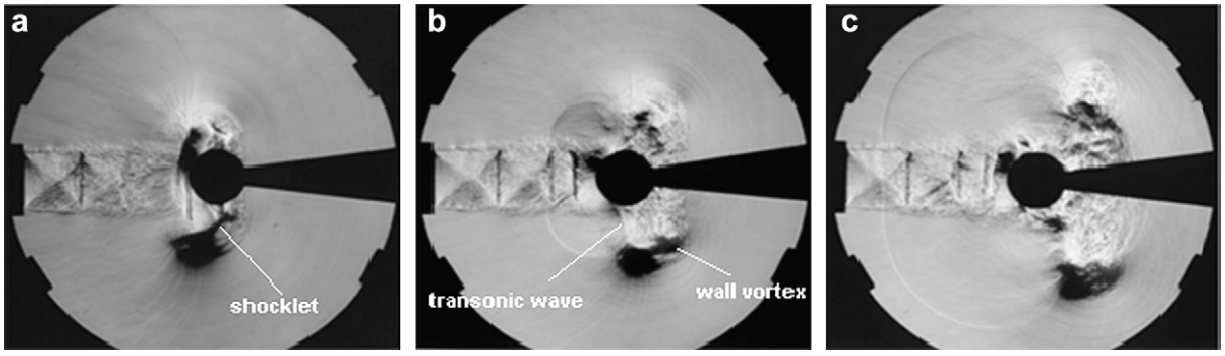

Fig. 20. Schlieren images showing the interaction of the vortex ring with a sphere at (a) 1.7 ms, (b) 1.8 ms and (c) 1.9 ms for a shock Mach number of 1.51.

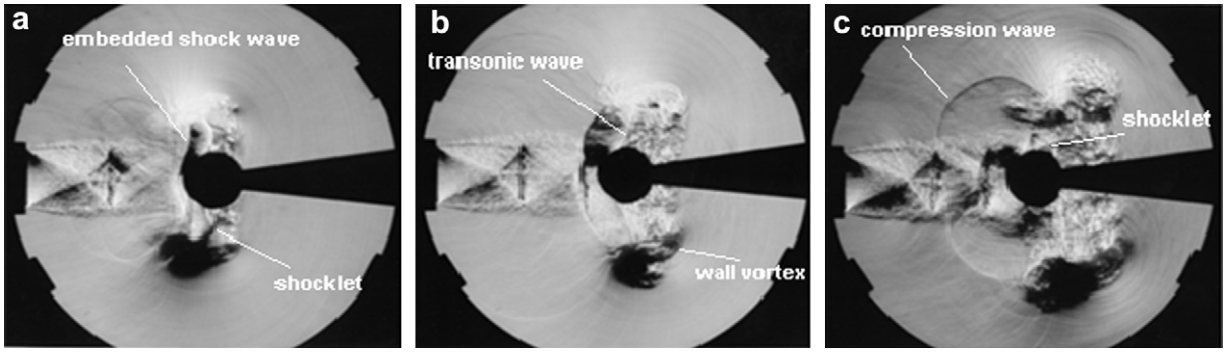

Fig. 21. Schlieren images showing the interaction of the vortex ring with a sphere at (a) 1.5 ms, (b) 1.6 ms and (c) 1.7 ms for a shock Mach number of 1.63.

the growth of the boundary layer on the cylinder. The continuous increase in pressure induces the separation of the boundary layer on the wall, resulting to the formation of the wall vortex. The decrease of pressure levels at time D is because of the presence of the wall vortex. The time of pressure variation (time D) is found to be consistent with the presence of the wall vortex shown in Figs. 13–15. Then, there is a number of further pressure fluctuations, as a result of the interactions that occur in the near-wall region. The pressure fluctuations are found to increase further in strength mainly due to the interaction of the cylinder with the jet (Fig. 17) and their duration is in agreement with the schlieren images shown in Figs. 13–15.

The pressure variations on either side of the stagnation region (Figs. 17 and 18), indicate that initially, the effect of the shock wave is most significant at the locations (0, and ±16 mm) closer to the stagnation point. The outer locations, ±32 and ±48 mm, are subjected to the least influence from the shock wave, with pressures close to the ambient pressure. This could be attributed to the fact that the shock wave propagates in a spherical shape, affecting mostly the wall pressure levels near the stagnation region. In addition, by the time the outer portions of the shock wave make contact with the plate, the shock wave has increased in radius and has become weaker so its effects are less pronounced in the outer regions.

4.2.2. Sphere

As the vortex ring approaches the apex of the sphere, a wall vortex is induced on the body with the vorticity in the opposite sense to that of the incident vortex ring (Figs. 19a, 20b and 21c. The impinging vortex is accelerated in the radial direction. The rate of growth in the radial direction is increasing with increasing driver pressure, but it is lower than that observed in the cylinder

configuration as the vortex ring is allowed to travel completely around the sphere. The wall vortex separates from the wall, rises up, winds around the main vortex (eventually reaches the same position as the main vortex) and merges with it (Figs. 19–21) – the presence of the wall vortex and its merging with the main vortex was also observed in the cylinder case as it can seen in Figs. 13–15. The merged vortex structure continues to rise, increases in diameter as it slows down and then diverges and dissipates.

The flow restriction produced by the wall vortex accelerates the flow between the wall vortex and the vortex ring to supersonic speeds and a shocklet is formed to satisfy the boundary condition as the pressure of the flow discharging through the narrow gap between the main and the wall vortex must be joined to the higher ambient pressure. The deceleration of the flow through this shock wave promotes even more the separation of the wall flow. This shocklet connects the cores of the two vortices and spherical acoustic waves are emitted around it. Further acoustic waves are emitted due to the collision and eventual merger of the two vortices (Figs. 19–21). The field described is similar to that produced by the head-on collision of two compressible vortex rings emanated from the open ends of two separate shock-tubes (Minota et al., 1998).

In the 3.95 bar case, a transonic wave is observed between the sphere and the core of the vortex ring, which strengthens with time. This wave is due to the local supersonic flow around the core of the vortex ring. The transonic wave stretches as the vortex ring moves downstream and is gradually weakening to be a sound wave (Fig. 19b).

In the 7.89 and 11.84 bar cases, initially the small vortex rings ahead of the main vortex interact with the induced wall vortex and additional shocklets are formed due to the induced constriction and flow compression. As the vortex ring approaches the sphere and stretches radially, the flow between the embedded shock wave and the wall compresses greatly. A transonic wave is then observed between the sphere and the wall vortex. The transonic wave between the sphere and the wall vortex stretches as the wall vortex rises and is weakening to be a sound wave (Figs. 20b and 21b. A limit is reached where the highly compressed flow pocket can not sustain itself and it bursts. A new compression wave is produced, which interacts with the vortex ring core, the jet flow and wall vortex (Figs. 19–21). The central portion of the shock wave is flatter due to the opposing motion of the jet flow. After the bursting of the compressed flow pocket, another shocklet is formed between the sphere and vortex ring core due to the local supersonic flow behind the expanding spherical shock wave. This shocklet stretches as the vortex ring propagates downstream and increases in diameter, and is weakening to be a sound wave. In all cases, the generated acoustic waves' intensity increases with compressibility.

The comparison of Figs.14b, 14c, 20b and 20c, indicates that the generated compression wave from the sphere travels faster than that from the cylinder. This is because the reflected shock from the cylinder is affected by the inherent 'two-dimensionality' of the geometry in the lateral direction along its leading edge, which causes a more complicated reflection, which decelerates the reflected shock wave. In contrast to the cylinder case, the coherent shape of the ring is maintained at longer times. This could be attributed to the fundamental difference in the geometry of the two bodies. Sphere allows the vortex ring to propagate around it without loosing its initial strength. On the other hand, in the case of the cylinder the vortex ring strength is weakened, since part of it expands in the lateral direction along its leading edge. By merging the observations of the present article with those by Kontis et al. (2006), it conjectured that the physics of interaction of a vortex ring with a cylinder body, can be described as a combination of the interaction of the ring with a sphere body of radius equal to the radius of the cylinder, and the ring with a solid flat plate of side length equal to the height of the cylinder.

5. Conclusions

The present study has revealed results of both flow visualisation (schlieren photography) and pressure measurements on the interaction of shock wave induced vortices with a cylinder and a sphere, and it brings some new elements of understanding on the physics of the shock interactions and of the vortex dynamics. Experiments have been carried out at three-shock Mach numbers i.e., 1.28, 1.51 and 1.63.

The schlieren photographs have shown that as the reflected shock wave impinges on the vortex ring, its shape is deformed. In the case of $M_s = 1.28$ and $M_s = 1.51$ the effects of interaction were found to be less pronounced than those for $M_s = 1.63$. However, the vortex ring appears to maintain its compact structure for all shock Mach number cases examined. At the higher shock Mach number case, multiple layers of shock waves were generated.

As the vortex approaches the cylinder, part of it accelerates rapidly in the lateral direction along the leading edge of the body, whereas remaining flow moves around the cylinder. The surface pressure measurements indicated that as the flow starts to spread laterally the pressure levels were reduced. Then, the sharp increase of the pressure levels indicates the growth of the boundary layer on the cylinder. The continuous increase in pressure induces the separation of the boundary layer on the wall, resulting to the formation of the wall vortex of opposite vorticity, which approaches the primary vortex. The two vortices merge together before they finally diverge and dissipate. The strength of these phenomena is found to increase as the shock Mach number increases from 1.28 to 1.63. In addition, the flow visualisation images have shown that a region of strong flow development is generated near the wall surface causing a reflected wave towards the shock-tube. The presence of this region was found to produce multiple pressure fluctuations on the wall of increasing magnitude. The pressure variations increase further due to the jet flow behind the ring reaching a maximum value. Then, pressure starts to decay indicating dissipation of the flow-field. The pressure measurements are found to be consistent with the schlieren images.

As the vortex ring approaches the apex of the sphere, a wall vortex is induced on the body with the vorticity in the opposite sense to that of the incident vortex ring. The impinging vortex is accelerated in the radial direction. The rate of growth in the radial direction is increasing with increasing driver pressure, but it is lower than that observed in the cylinder configuration as the vortex ring is allowed to travel completely around the sphere. The wall vortex separates from the wall, rises up, winds around the main vortex (eventually reaches the same position as the main vortex) and merges with it. The merged vortex structure continues to rise, increases in diameter as it slows down and then diverges and dissipates. A transonic wave is observed between the sphere and the core of the vortex ring, which strengthens with time. The transonic wave stretches as the vortex ring moves downstream and is gradually weakening to be a sound wave. The generated compression wave from the sphere travels faster than that from the cylinder. In contrast to the cylinder case, the coherent shape of the ring is maintained at longer times. It is conjectured that the physics of interaction of a vortex ring with a cylinder body, can be described as a combination of the interaction of the ring with a sphere body of radius equal to the radius of the cylinder, and the ring with a solid flat plate of side length equal to the height of the cylinder.

Acknowledgements

The authors are indebted to the technical staff at The University of Manchester for their assistance. The technical support of Dr. J.A. Edwards and EPSRC is greatly acknowledged.

References

Arakeri, J.H., Das, D., Krothapalli, A., Lourenco, L., 2004. Vortex ring formation at the open end of a shock tube: a particle image velocimetry study. Physics of Fluids 16, 1008–1019.

Baird, J.P., 1987. Supersonic vortex rings. Proceedings of Royal Society of London, Series A 409, 59–65.

Ben-Dor, G., 1992. Shock Wave Reflection Phenomena. Springer-Verlag.

Ben-Dor, G., Takayama, K., Kawauchi, T., 1980. The transition from regular to mach reflexion and from mach to regular reflexion in truly non-stationary flows. Journal of Fluid Mechanics 100, 147–160.

Bleakney, W., Weimer, D.K., Fletcher, C.H., 1949. The shock tube: a facility for investigations in fluid dynamics. The Review of Scientific Instruments 20, 807–815.

Brouillette, M., Hebert, C., 1997. Propagation and interaction of shock-generated vortices. Fluid Dynamics Research 21, 159–169.

Bryson, A.E., Gross, R.W.F., 1960. Diffraction of strong shocks by cones, cylinders and spheres. Journal of Fluid Mechanics 10, 1–16.

Courant, R., Friedrichs, K.O., 1948. Supersonic Flow and Shock Waves. Interscience, New York.

Elder, F.K., De Haas, N., 1952. Experimental study of the formation of a vortex ring at the open end of a cylindrical shock tube. Journal of Applied Physics 23, 1065–1069.

Emrich, R.J., Curtis, C.W., 1953. Attenuation in the shock tube. Journal of Applied Physics 24, 360–363.

Emrich, R.J., Wheeler, D.B., 1958. Wall effects in shock tube flow. Physics of Fluids 1, 14–23.

Glass, I.I., Sislian, J.P., 1994. Nonstationary Flows and Shock Waves. Oxford University Press.

Gonor, A.L., Gottlieb, J.J., Hooton, I., 2004. Shock wave diffraction over wedges, cylinders and spheres in gases, liquids and condensed matter. Journal of Applied Physics 95, 1577–1585.

Heilig, W.H., 1969. Diffraction of a Shock Wave by a Cylinder. The Physics of Fluids Supplement I, 154–157.

Kontis, K., An, R., Edwards, J.A., 2006. Compressible vortex-ring interaction studies with a number of generic body configurations. AIAA Journal 44 (12), 2962–2978.

Merzkirch, W., 1974. Flow Visualization. Academic Press Inc..

Minota, T., Nishida, M., Lee, M.G., 1998. Head-on collision of two compressible vortex rings. Fluid Dynamics Research 22, 43–60.

Settles, G., 2001. Schlieren and Shadowgraph Techniques: Visualizing Phenomena in Transparent Media. Springer-Verlag, Berlin and Heidelberg GmbH and Co.

Shugaev, F.V., Shtemenko, L.S., 1998. Propagation and reflection of shock waves. Series on Advances in Mathematics for Applied Sciences, vol. 49. World Scientific.

Sun, M., Saito, T., Takayama, K., Tanno, H., 2005. Unsteady drag on a sphere by shock wave loading. Shock Waves 14, 3–9.

Tanno, H., Itoh, K., Saito, T., Abe, T., Takayama, K., 2003. Interaction of a shock with a sphere suspended in a vertical shock tube. Shock Waves 13, 191–200.

Tokugawa, N., Ishii, Y., Sugano, K., Takayama, F., Kambe, T., 1997. Observation and analysis of scattering interaction between a shock wave and a vortex ring. Fluid Dynamics Research 21, 185–199.

Von Neumann, J., 1963. Collected Works. Pergamon Press.

White, D.R., 1958. Influence of diaphragm opening time on shock-tube flows. Journal of Fluid Mechanics 4, 585–599.

Whitham, G.B., 1957. A new approach to problems of shock dynamics part i two-dimensional problems. Journal of Fluid Mechanics 2, 145–171.

Yang, J.Y., Liu, Y., Lomax, H., 1987. Computation of shock wave reflection by circular cylinders. AIAA Journal 25, 683–689.